Journal of Advanced Ceramics

*J Adv Ceram* 2025, **14**: 9221189

https://doi.org/10.26599/JAC.2025.9221189

Research Article

Orbital hybridization and charge distribution modulation in MOF-derived

carbon materials for tailored electromagnetic attenuation

Yuan Liu <sup>1, ∞</sup>, Muhe Li <sup>1</sup>, Rong Li <sup>1</sup>, Yuchang Qing <sup>2, ∞</sup>, Long Wang <sup>2</sup>, Bingbing Fan <sup>3, ∞</sup>

<sup>1</sup> Rocket Force University of Engineering, Xi'an 710025, China

<sup>2</sup> State Key Laboratory of Solidification Processing, School of Material Science and Engineering,

Northwestern Polytechnical University, Xi'an 710072, China

<sup>3</sup> College of Material Science and Engineering, Zhengzhou University, Zhengzhou 450001, China

⊠ Corresponding author.

E-mail: Y. Liu, liuyuanbixue@163.com;

Y. Qing, qtvbgyta@163.com, qingyuchang@nwpu.edu.cn;

B. Fan, fanbingbing@zzu.edu.cn

Received: August 11, 2025; Revised: September 17, 2025; Accepted: October 4, 2025

©The Author(s) 2025

**Abstract:** Despite the extensive research conducted on dielectric-magnetic coupling in MOF-derived

absorbers, the underlying mechanisms associated with defects, interfaces, and orbital hybridization

remain inadequately investigated. To address this, we developed coral-like MOF-derived nickel-

phosphorous@carbon (NP@C) nanocomposites by adjusting the pyrolysis temperature, revealing for

1

Journal of Advanced Ceramics

https://mc03.manuscriptcentral.com/jacer

the first time the link between structure and electromagnetic (EM) performance. The composite

features nickel phosphide nanoparticles (Ni<sub>12</sub>P<sub>5</sub> core/Ni<sub>2</sub>P shell) embedded in an amorphous carbon

matrix, where unique crystal orientation and interfacial coupling enhance EM wave dissipation.

Calculations show that charge transfer (0.66 e) at the C-Ni<sub>12</sub>P<sub>5</sub> interface boosts conductance loss,

while the C-Ni<sub>2</sub>P-Ni<sub>12</sub>P<sub>5</sub> heterostructure generates interfacial polarization and defect states via

negative charge transfer (0.20 e), synergistically enhancing dielectric and magnetic loss. Electronic

structure analysis reveals that sharp Ni 3d orbital peaks near the Fermi level coexist with broad

carbon matrix peaks, enabling both conductive and spin-related magnetic loss mechanisms. The

NP@C nanocomposite achieves a reflection loss of -54.1 dB and an effective absorption band

covering 4.1 GHz at a thin thickness of 1.37 mm. This study clarifies the atomic- and electronic-level

EM response mechanisms of MOF-derived carbon materials, offering new insights for designing

high-performance absorbers.

Keywords: Metal-organic frameworks; interfacial polarization; conductance loss; magnetic loss;

electromagnetic wave absorption

Introduction

The proliferation of next-generation electronics, including 5G/6G systems, IoT, and wearables, has

dramatically increased human exposure to artificial electromagnetic (EM) waves. These EM waves,

particularly in the microwave and radiofrequency ranges, have been linked to potential biological

hazards, including DNA damage, oxidative stress, and neurological disorders [1–3]. Moreover, EM

interference disrupts the normal operation of sensitive electronic equipment, affecting

communication accuracy, medical diagnostics, and aerospace systems [4, 5]. To mitigate these issues,

the development of high-performance absorbers has become a critical research focus.

Among diverse candidate absorbers, metal-organic framework (MOF) - derived carbon materials

2

have emerged as particularly promising candidates owing to their exceptional structural adaptability that facilitates precise modulation of EM characteristics [6-8]. MOFs represent a class of crystalline porous coordination polymers formed through the spontaneous organization of metal clusters and multifunctional organic linkers. Their well-defined periodic architectures endow these materials with extraordinary specific surface areas, tunable pore geometries, and abundant active sites [9, 10]. More importantly, the chemical composition (e.g., types of metal nodes and ligand structures) and topological dimensions (1D, 2D, or 3D) of MOFs can be precisely regulated under controlled synthesis conditions, facilitating the directional design of dielectric and magnetic loss characteristics [11-13]. For instance, the pyrolysis of zeolitic imidazolate frameworks (ZIFs) centered on Zn or Co yields carbon-based composites with high dielectric loss [14, 15], whereas MIL-series MOFs containing Fe or Cr tend to produce iron-based oxides with magnetic loss properties [16-18]. Additionally, strategies such as solvothermal synthesis, surfactant-assisted fabrication, or temperature regulation allow further optimization of MOF crystal orientation and microscopic morphology (e.g., core-shell structures, hollow polyhedra, or layered porous architectures), thereby enhancing multiple scattering and impedance matching characteristics of EM waves [19, 20].

The pyrolytic transformation of MOFs is a critical step in obtaining high-performance absorbers. By precisely controlling pyrolysis conditions (e.g., temperature, atmosphere, and heating rate), MOF precursors can be converted into multi-component composite materials, including metal/carbon hybrids, metal oxides, sulfides, or ferrites [21-23]. These materials typically exhibit significant synergistic effects. The carbon matrix provides high electrical conductivity and dielectric loss, while magnetic components (e.g., Fe<sub>3</sub>O<sub>4</sub>, CoNi alloys) contribute to magnetic loss [24-26]. For example, Che et al. reported that the octadecahedral Co@N-doped carbon material achieved an effective absorption bandwidth (EAB) of 6.2 GHz at a thickness of 1.8 mm [27]. Similarly, Lu et al. developed Fe&TiO<sub>2</sub>@C composites that exhibit strong absorption capabilities due to multiple interfacial polarizations [28]. These achievements underscore the immense potential of MOF-derived

Journal of Advanced Ceramics materials in EM protection applications.

Despite significant progress in experimental research on MOF-derived absorbers, the physical mechanisms underlying performance optimization remain inadequately explained. Most existing studies focus on characterizing macroscopic parameters (e.g., complex permittivity and permeability), while insufficient attention is paid to the correlation between the microscopic electronic structure of materials (e.g., charge distribution, energy band characteristics, and density of states) and EM response properties [29, 30]. This cognitive gap severely hinders the rationalization of material design. Specifically, the intrinsic EM wave absorption mechanism of magnetic carbon materials involves complex multi-scale physical processes. At the atomic scale, charge transfer at the metal-carbon hybrid interface may induce local dipole polarization. At the nanoscale, the size effect and dispersion of magnetic particles influence magnetic domain wall resonance. At the microscopic scale, multiple reflections caused by porous structures enhance EM energy dissipation [31, 32]. Traditional experimental methods struggle to directly observe these microscopic phenomena, whereas theoretical simulations offer a crucial perspective for elucidating structure-property relationships. Notably, the related EM performances relying on the electronic/atomic structure of MOF-derived absorbers have not been explored.

Herein, we report the coral-like MOF-derived nickel-phosphorous@carbon (NP@C) nanocomposites by combining liquid-phase diffusion and high-temperature pyrolysis. Through density functional theory (DFT) calculations, we analyzed the electron density of states (DOS), charge density difference (CDD), and band structure of representative NP@C nanocomposite (e.g., C-Ni<sub>12</sub>P<sub>5</sub>, C-Ni<sub>2</sub>P-Ni<sub>12</sub>P<sub>5</sub>), clarifying the contribution of charge distribution at the metal-carbon interface to dielectric polarization. The local coordination environment of Ni in coral-like NP@C materials is analyzed by using X-ray Absorption Fine Structure (XAFS) spectroscopy. This work reveals for the first time the interdependent relationship between the electronic structure and

## 2 Experimental section

Reagents: 4, 4'-bismaleimide diphenylmethane (C<sub>21</sub>H<sub>14</sub>N<sub>2</sub>O<sub>4</sub>, 98%, BDM), 2, 2'-diallyl bisphenol (C<sub>21</sub>H<sub>24</sub>O<sub>2</sub>, 90%, DBA) and phenylbis (2, 4, 6-trimethylbenzoyl) phosphine oxide (C<sub>26</sub>H<sub>27</sub>O<sub>3</sub>P, 97%) were purchased from Anage Chemical Co., LTD. 1-vinyl-2-pyrrolidone (C<sub>6</sub>H<sub>9</sub>NO, 99%, containing 100 ppm NaOH stabilizer), N, N-dimethylcarbamide (C<sub>3</sub>H<sub>7</sub>NO, 98%) Nickel nitrate hexahydrate (Ni(NO<sub>3</sub>)<sub>2</sub>•6H<sub>2</sub>O, 99.99%) was obtained from Shanghai Aladdin Biochemical Co., Ltd.

Preparation of MOF precursor: 20.0 g DBA, 2.0 g Ni(NO<sub>3</sub>)<sub>2</sub>•6H<sub>2</sub>O and 20.0 g DMF were added to a beaker, and was heated it to 135 °C. Next, 27.6 g BDM was added to the above liquor, and vigorously stirred violently until BDM was completely dissolved, then reduced the temperature to 60 °C. After that, by adding 2.0 g C<sub>26</sub>H<sub>27</sub>O<sub>3</sub>P and 20.0 C<sub>6</sub>H<sub>9</sub>NO, the mixed solution was placed in the ultraviolet environment for 30 min to obtain the MOF precursor.

MOF-derived nickel-phosphorous@carbon (NP@C) nanocomposites: The obtained MOF precursor was placed heated at 5 °C/min to a preset temperature (800 °C, 900 °C and 1000 °C) and kept in flowing argon for 4 h. It should be inferred that magnetic materials consisting of Ni<sub>2</sub>P/Ni<sub>12</sub>P<sub>5</sub> nanoparticles embedded within a carbon matrix (denoted as NP@C). According to the heating temperature, the prepared samples were designated as NP@C-800, NP@C-900, and NP@C-1000, respectively.

Characterization: The crystalline structure of MOF-derived NP@C nanocomposites was inspected by X-ray Diffraction (XRD, Netherlands, PANalytical B.V., X'Pert PRO). Morphologies were observed by SEM, HR-TEM and Cs-corrected TEM. The band gap of the material was measured by Ultraviolet and Visible Spectrophotometry (UV-vis, Japan-Shimadsu-UV-3600 plus). To investigate the EM properties of the products, the as-prepared samples and paraffin wax were cut into a ring shape with the outer diameter of 7.0 mm and the inner diameter of 3.04 mm. The EM parameter was

determined by vector network analyzer (VNA, Agilent E8362B, America). In this work, 40 wt%

NP@C products were evenly mixed with paraffin wax matrix and measured in 2-18 GHz. The radar cross section (RCS) plots were simulated by means of CST Studio Suite.

First-principles calculations were performed within the framework of density-functional theory (DFT) as implemented in the Vienna ab initio simulation package (VASP). Electronic structure calculations were performed using periodic DFT within the CP<sub>2</sub>K software package, utilizing its Gaussian and plane wave basis set implementation in the Quickstep module. The exploratory study of the catalyst structure employed the molecular-optimized basis sets DZVP-MOLOPT-SR-GTH for each atom and the Goededec-Teter-Hutter (GTH) pseudopotential. We implemented the PBE-GGA exchange-correlation functional with van der Waals corrections (DFT-D3), enforcing an SCF convergence threshold of 5×10<sup>-6</sup> Hartree for all calculations. An energy truncation value of 400 Ry was used throughout the calculation process. The input file is generated by Multiwfn.

## 3 Results and Discussion

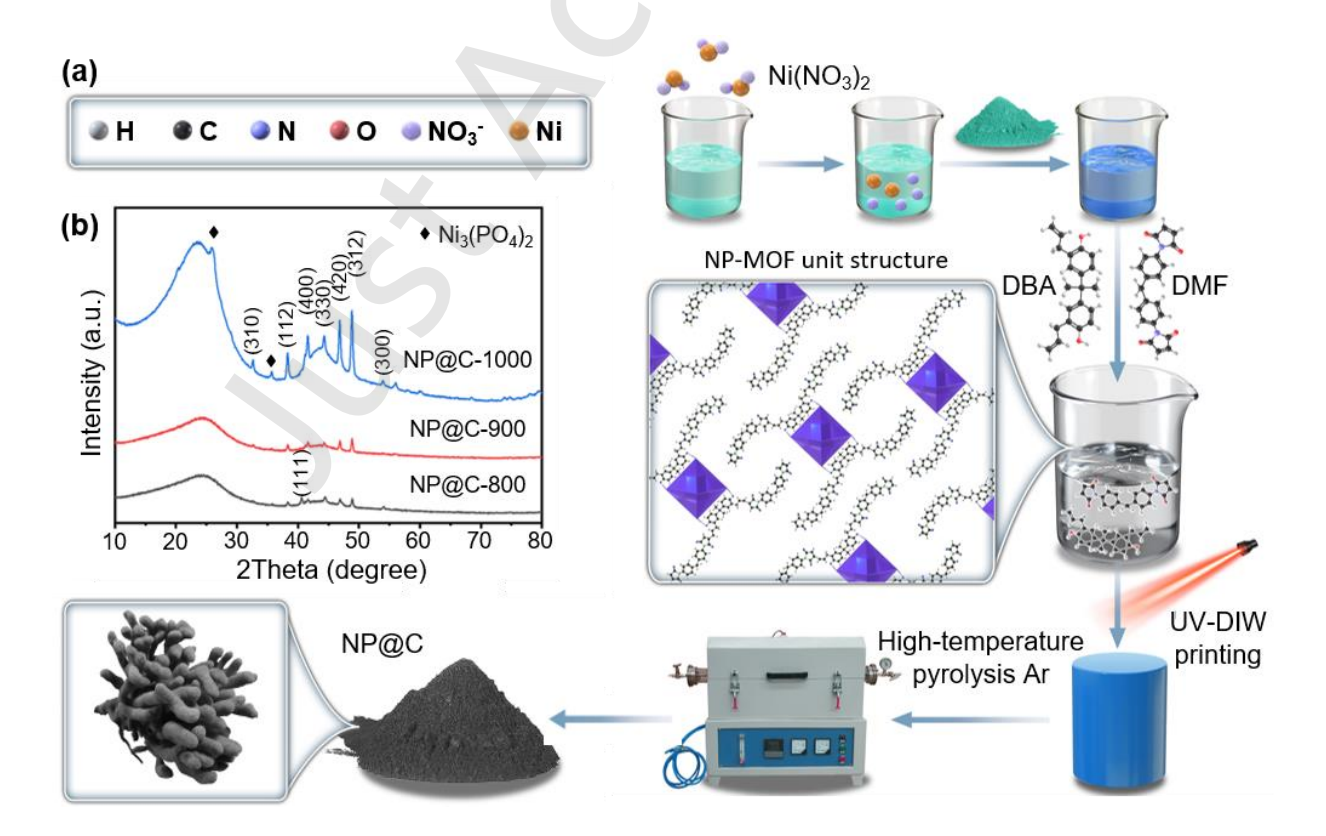


Fig. 1 Illustration the procedure. Schematic diagram of (a) the synthesis process and (b) XRD

patterns of MOF-derived NP@C absorbents obtained at different reduction temperatures.

At the atomic scale, the analysis of chemical properties and coordination of MOF-derived nickelphosphorous@carbon (NP@C) phases is crucial for adjusting cell fraction and grain boundaries. In this work, the synthetic procedure for NP@C is initially demonstrated in Fig. 1. The MOF precursor was first prepared by the liquid phase diffusion method, and then hydrogenated to obtain coralloid NP@C products at different temperatures ranging from 800 to 1000 °C (Fig. 1a). Typically, the MOF precursor can be formed through the coupling of metallic Ni ions with organic ligands. Fig. 1b illustrates the XRD pattern of the MOF-derived NP@C nanocomposites with different pyrolysis temperatures. The distinct peak clusters of NP@C samples emerge after high-temperature calcination, suggesting a presence of amorphous carbon. Simultaneously, the diffraction peak intensity is high due to the thin carbon layer on the surface of NP@C nanocomposites. The diffraction peaks of (310), (112), (400), (330), (420) and (312) crystal planes are corresponding to Ni<sub>12</sub>P<sub>5</sub> (JCPDS card No. 74-1381) [33]. The diffraction peaks of (111) crystal plane is belonged to Ni<sub>2</sub>P (JCPDS card No. 03-0953) and the characteristic peaks of Ni<sub>3</sub>(PO<sub>4</sub>)<sub>2</sub> (JCPDS card No. 70-1796) appear around 2 Theta =  $25.9^{\circ}$  and  $35.5^{\circ}$  region [34]. The XRD patterns show that the crystallinity of the samples improves significantly with increasing calcination temperature, as evidenced by the sharpening and intensification of the diffraction peaks.

Raman spectroscopy was performed to investigate defects or disordered structures in NP@C nanocomposites prepared at different pyrolysis temperatures (Fig. 2a). The Raman spectrum of the composite exhibits two characteristic bands at 1350 cm<sup>-1</sup> (D-band) and 1580 cm<sup>-1</sup> (G-band), corresponding to disordered carbon structures and graphitic domains, respectively. The intensity ratio ID/IG of the characteristic peaks can characterize the defect degree of carbon materials to a certain extent. The higher the ratio, the greater the defect density. The ID/IG values of NP@C-800 ~ NP@C-1000 samples are 0.56, 0.69 and 1.17, respectively. Graphite is highly ordered with an ID/IG close to 0, while the reduced graphene oxide (rGO) group has high defects with an ID/IG typically

https://mc03.manuscriptcentral.com/jacer Journal of Advanced Ceramics ranging from 1.0 to 1.5. The graphitization of NP@C-800 and NP@C-900 is between that of graphite and rGO, while NP@C-1000 is more inclined towards graphene oxide. Ni, as the magnetic component, attenuates EM waves through natural resonance and eddy current loss. The carbon matrix in NP@C-800 is highly ordered and the conductive network is relatively complete. This structure mainly generates conductive loss through the migration of free electrons, but the interfacial polarization effect is relatively weak, resulting in dielectric loss mainly relying on the conductivity of the material itself. NP@C-900 product introduces moderate defects. These defects not only enhance the dielectric loss through the relaxation polarization of the sp<sup>2</sup>/sp<sup>3</sup> hybrid interface, but also may serve as anchor sites for Ni particles, optimizing the interfacial coupling between the magnetic components and the carbon matrix. NP@C-1000 is a high-defect carbon matrix, in which the carbon matrix has a large number of disordered structures and defects. The high defect density significantly enhances the interfacial polarization effect, thereby greatly increasing the dielectric loss. However, too many defects disrupt the continuity of the carbon skeleton, resulting in reduced conductivity and weakening the contribution of conductance loss. Therefore, under the synergy of polarization loss and electrical loss, NP@C-900 sample maybe more suitable for wideband absorption.

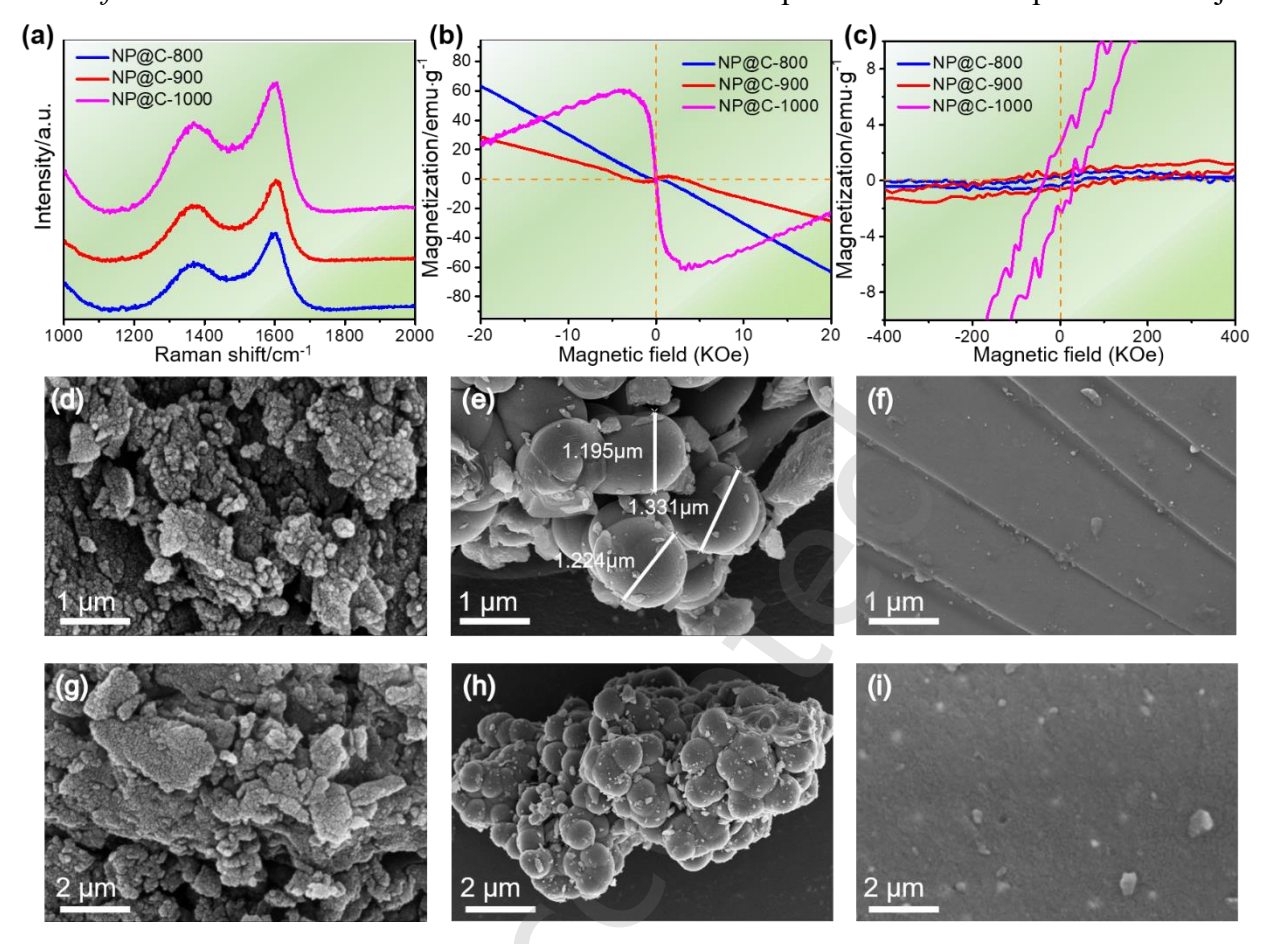


**Fig. 2** Structure and morphology characterizations. (a) Raman spectrum, (b, c) VSM curves of MOF-derived NP@C nanocomposites. The low- and high-magnified SEM images of (d, g) NP@C-800, (e, h) NP@C-900 and (f, i) NP@C-1000 materials.

Fig. 2 (b, c) shows the hysteresis loop of NP@C materials, which exhibits typical ferromagnetic properties. The saturation magnetization intensities (Ms) of the NP@C-800 ~ NP@C-1000 samples are 63.29, 28.34 and 23.14 emu·g<sup>-1</sup>, respectively. The ferromagnetism in the composite materials mainly comes from the magnetic metal Ni and its compounds. As the pyrolysis temperature increases, the crystal structure of NP@C becomes more obvious, increasing the magnetization intensity and eventually causing the Ms to show a decreasing trend. NP@C-800 sample exhibits the hysteresis effect of magnetic materials, and with the increase of pyrolysis temperature NP@C-800 shows multiple magnetic phases, but due to its lower magnetic saturation point and faster rate of change, it may be unfavorable for EM wave loss. In Fig. 2(d, g), NP@C-800 presents an irregular

Journal of Advanced Ceramics

https://mc03.manuscriptcentral.com/jacer
granular structure at the nanoscale, with an uneven size distribution. The granular structure keeps
decreasing, and after the material decomposes, it continuously combines to form a blocky structure.

NP@C-900 shows a regular spherical structure, with a size of approximately 1.1-1.4 µm (Fig. 2(e,
h)). Meanwhile, obvious agglomeration occurs between the spherical structures. When the pyrolysis
temperature rises to 1000°C, the spherical structures decompose and recombine to form relatively
smooth planes, as shown in Fig. 2(f, i). This structure is not conducive to the entry of EM waves into

the interior of the structure.

To further analyze the microstructure of the composites, TEM analysis was performed on NP@C-900 and NP@C-1000. In Fig. 3(a-c), the NP@C-900 sample is composed of amorphous carbon and a large number of Ni nanoparticles distributed within it. This indicates that after high-temperature pyrolysis, the metal atoms undergo agglomeration. While the carbon layer plays a connecting and supporting role among the nanoparticles, it also forms a conductive network system among the metal particles. When the incident electron beam direction of the NP@C-900 sample is aligned with the crystal zone axis, the interplanar spacings of 0.22 nm, 0.19 nm, and 0.30 nm correspond to the (2-20), (-1-1-2), and (1-3-2) crystal planes of Ni<sub>12</sub>P<sub>5</sub>, respectively [35]. In Fig. 3 (d, e), the diffraction ring belongs to Ni<sub>12</sub>P<sub>5</sub>, and the diffraction points belong to the crystal plane of (2-3-1), (11-2) and (-14-1). Ni-based nanoparticles are mainly composed of Ni<sub>12</sub>P<sub>5</sub> and Ni<sub>2</sub>P. In Fig. 3 (f-h), when the pyrolysis temperature rises to 1000°C, Ni nanoparticles decompose and disperse in the uncertain carbon, but their crystal structure does not change significantly and is still dominated by Ni<sub>12</sub>P<sub>5</sub>. Fig. 3 (i-l) shows the elemental mapping of NP@C-900 material. It can be clearly seen that the distribution of Ni and P is consistent with the contour of the TEM image. Ni and P together form NP@C nanoparticles. The other elements are uniformly distributed in the NP@C-900 material. There is no agglomeration of elements in any place.

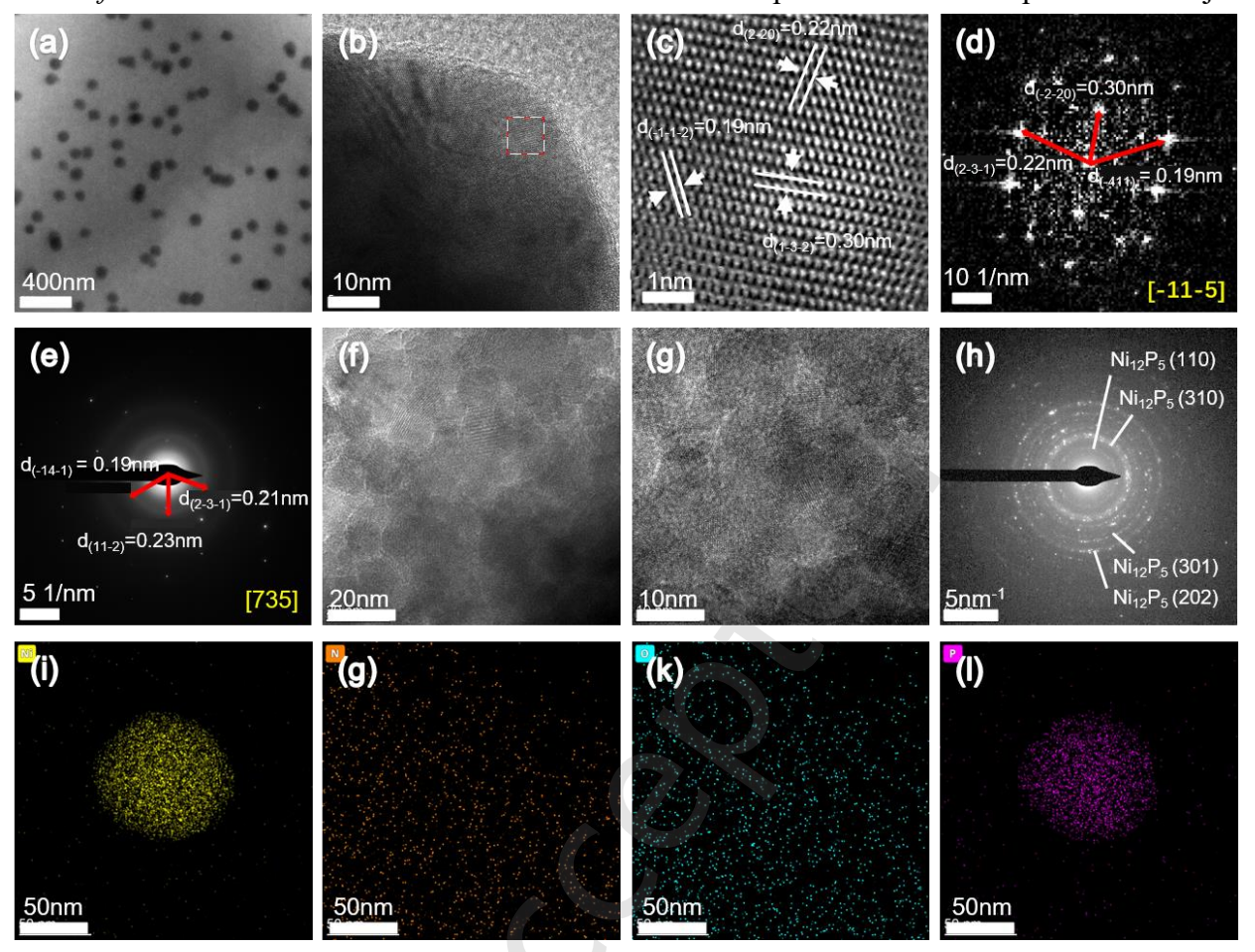


**Fig. 3** The microstructure of NP@C samples. (a, b) TEM images, (c) Fourier transform diffraction analysis of the region in Fig. 3b, (d, e) SAED spectra and (i-l) Corresponding element mapping results of Ni, N, O and P of NP@C-900 sample. (f, g) TEM images and (h) SAED spectrum of NP@C-1000 sample.

In Fig. 4, the EM parameters of MOF-derived NP@C nanocomposites were tested in the frequency of 2 - 18 GHz. In Fig. 4(a-c), the  $\varepsilon'$  values of the NP@C samples gradually increase as the pyrolysis temperature enhanced. Meanwhile, the  $\varepsilon'$  values of the NP@C samples show a fluctuating downward trend, while the  $\varepsilon''$  values of the samples fluctuate more. However, when the pyrolysis temperature rises to  $1000^{\circ}$ C, the  $\varepsilon''$  decreases sharply and tends to 0. It could be inferred that the formation of coral-like structure in the material promotes the formation of conductive network. After the pyrolysis temperature increases, the value of the NP@C sample first increases and then decreases, and the degree of fluctuation decreases at the same time. This is mainly because the

Journal of Advanced Ceramics https://mc03.manuscriptcentral.com/jacer change in the material morphology forms numerous heterogeneous interfaces, enhancing the interfacial polarization and conductance loss. In addition, when the pyrolysis temperature reached 900°C, three resonance peaks gradually appeared in the composite, more than at the other two pyrolysis temperatures, indicating the presence of more multipolarization losses in NP@C-900,

which to some extent contributed to the improvement of absorbing capacity of the material.

In Fig. 4(g-i), the  $\mu'$  value of the sample increases gradually with the rise of temperature, but when the pyrolysis temperature is 800°C, the  $\mu'$  value is higher than that of the sample with higher pyrolysis temperature at low frequencies and lower than that of NP@C-900 at high frequencies. The value of NP@C-800 fluctuates between 0.95 and 1.35. The  $\mu''$  values of the samples fluctuated between 0 and 0.3, showing a trend of first decreasing and then increasing. When the pyrolysis temperature increases, the variation trend of the  $\mu''$  values is that the fluctuation amplitude first decreases and then increases. However, when the pyrolysis temperature rises to 1000°C, the  $\mu''$  value increases significantly, and the fluctuation frequency increases, but the fluctuation amplitude decreases. The change of the sample is obvious, indicating that the influence of dielectric EM loss on the material is relatively small. Its regulatory effect on the absorbing ability is mainly reflected in the influence on the dielectric constant, with polarization loss being the main factor. When the pyrolysis temperature further increases, the tan  $\delta_{\mu}$  value of the NP@C-1000 sample rises, the magnetic components increase, and the magnetic loss capacity of the material will be enhanced to a certain extent. However, when the temperature is too high, the magnetic components decrease, and its magnetic loss capacity will be weakened to a certain extent.

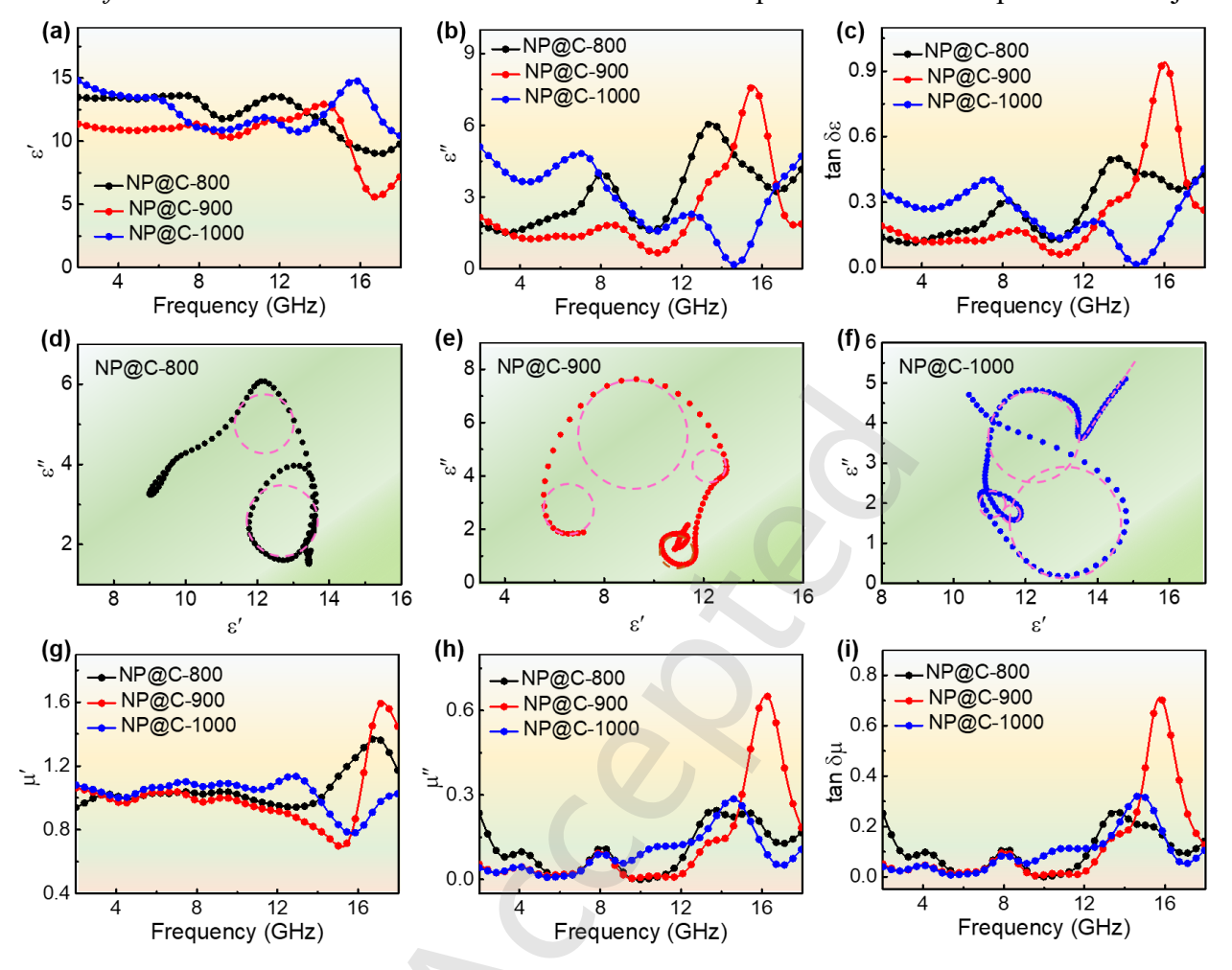
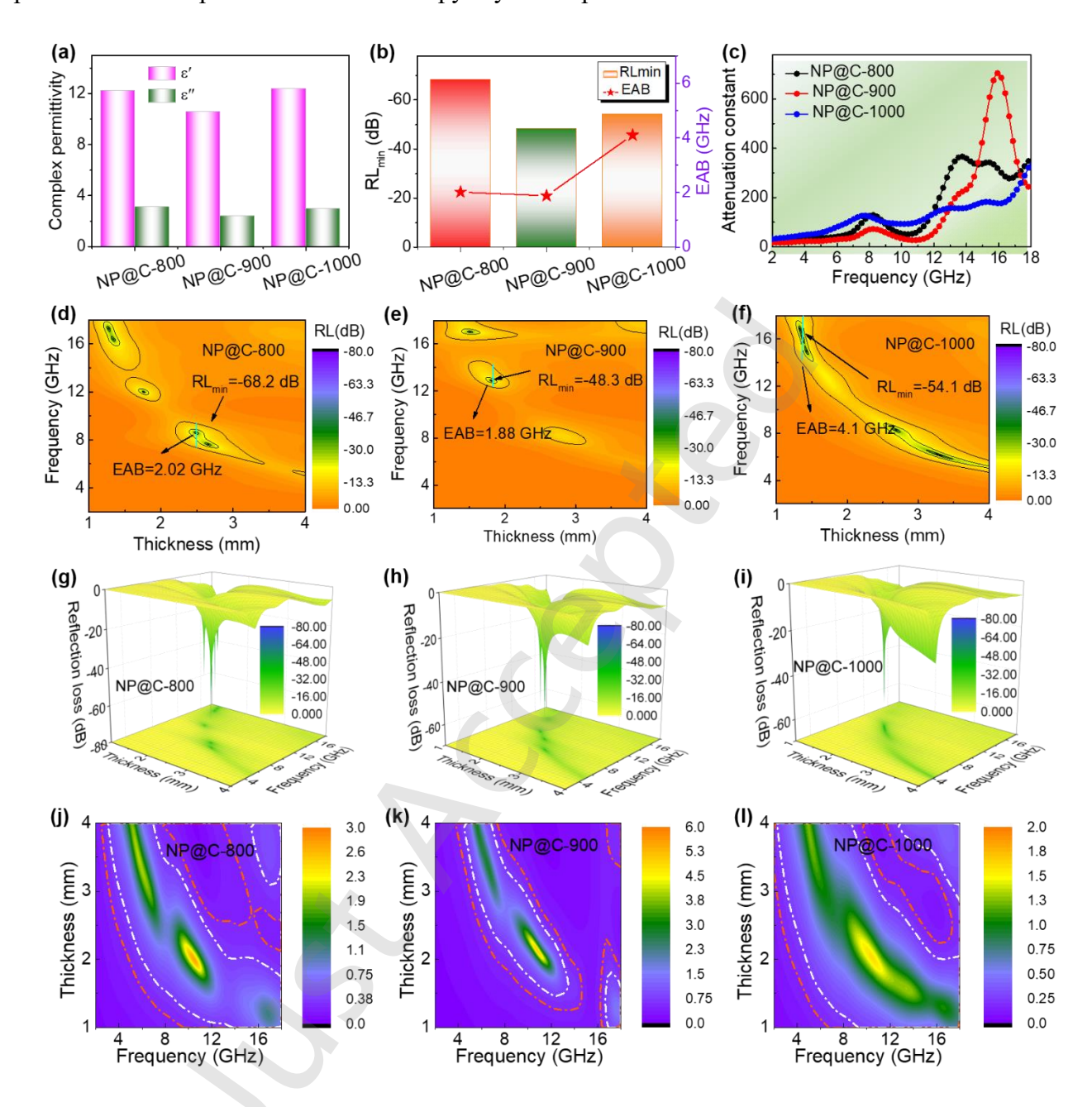


Fig. 4 Electromagnetic performance. (a)  $\epsilon'$ , (b)  $\epsilon''$  and (c)  $\tan \delta_{\epsilon}$  values of NP@C materials. Cole-Cole curves of (d) NP@C-800, (e) NP@C-900 and (f) NP@C-1000. (g)  $\mu'$ , (h)  $\mu''$  and (i)  $\tan \delta_{\mu}$  values of NP@C materials.

Fig. 5 shows the reflectance plots and 3D reflectance plots of NP@C at different pyrolysis temperatures. For NP@C-900, there is an effective absorption of less than −10 dB within the frequency ranges of 7.34-9.36 GHz (2.02 GHz), and the minimum reflective loss (RL<sub>min</sub>) is −68.2 dB at 8.6 GHz (2.49 mm) (Fig. 5(d, g)). The RL<sub>min</sub> of NP@C-900 reaches to −48.3 dB at 12.9 GHz (1.81 mm), and the corresponding EAB is 1.88 GHz (12.34-14.22 GHz) (Fig. 5(e, h)). When the pyrolysis temperature rises to 1000°C, the RL<sub>min</sub> of NP@C-1000 is −54.1 dB at 16.1 GHz (1.37 mm), and the corresponding EAB is 4.1 GHz (13.9-18.0 GHz) (Fig. 5(f, i)). To sum up, NP@C-1000 achieves a smaller peak reflectance and a larger effective bandwidth, and has better wave absorption

performance compared to the other two pyrolysis temperatures.



**Fig. 5** EM wave absorption performance. (a) The average values of the complex permittivity. (b) Summary of EAB and RL<sub>min</sub> for the samples. (c) Attenuation constant of different NP@C products. The frequency-dependence of 2D RL images for (d) NP@C-800, (e) NP@C-900 and (f) NP@C-1000. 3D images of the frequency-dependence RL with thicknesses of 0.5–4.0 mm of (g) NP@C-800, (h) NP@C-900 and (i) NP@C-1000. Impedance matching of (j) NP@C-800, (k) NP@C-900 and (l) NP@C-1000.

The differences in the absorbing properties of NP@C-800 ~ NP@C-1000 products are analyzed as follows. In Fig. 5c, the attenuation constant (α) value of NP@C increases firstly and then decreases with the increase of pyrolysis temperature. NP@C-900 sample exhibits the highest attenuation coefficient, which is attributed to the fact that as the carbonization temperature increases, the size of the conductive surface domain enlarges, resulting in higher conductivity, thus strengthening its conductivity loss.Fig. 5(j-l) shows the impedance matching values corresponding to different NP@C samples. The area of the NP@C-1000 sample that meets the normalized input impedance required for effective absorption (RL<-10 dB) is larger than that of the other samples. Therefore, it seems that the absorbing performance of these NP@C samples is related to the pyrolysis temperatures in view of their phase evolution. In short, among these annealing NP@C materials, the optimal NP@C-1000 sample is derived from the appropriate EM attenuation ability and best impedance matching.

To further analyze the atomic structure of NP@C composites, Cs-corrected TEM was used for observation. Because the surface of these materials is coated with a layer of carbon, the morphology, energy spectrum and corresponding crystal structure of NP@C-900 after cleaning are shown in Fig. 6. Fig. 6(a-c) show high-angle annular dark-field (HAADF) and annular bright-field (ABF) images of NP@C-900 sample. In Fig. 6b, the white area represents Ni nanoparticles and the black area represents amorphous carbon. It can be observed that the distribution of nanoparticles in amorphous carbon is relatively strong and the crystallinity is relatively high. The lattice fringes are distinct. In Fig. 6(c, d), the nanoparticles simultaneously contain two different crystal structures, with the inner layer being Ni<sub>12</sub>P<sub>5</sub> and the outer layer being Ni<sub>2</sub>P. Their atomic packing patterns belong to the tetragonal and hexagonal crystal systems respectively. It is composed of two elements, Ni and P, and its surface is covered with a carbon shell composed of amorphous carbon. Fig. 6(g, h) present the Cs-corrected TEM images of the samples and the corresponding atomic structure models of Ni<sub>12</sub>P<sub>5</sub>, showing the crystal structure of Ni<sub>12</sub>P<sub>5</sub>, which contains two oxidation states of Ni<sup>2+</sup> and Ni<sup>3+</sup>. Fig. 6g shows a P atom surrounded by six Ni atoms, presenting a triangular prismatic shape. The image

The element mapping results of the NP@C-900 materials consist of C, Co, P and O (Fig. 6(i-l)).

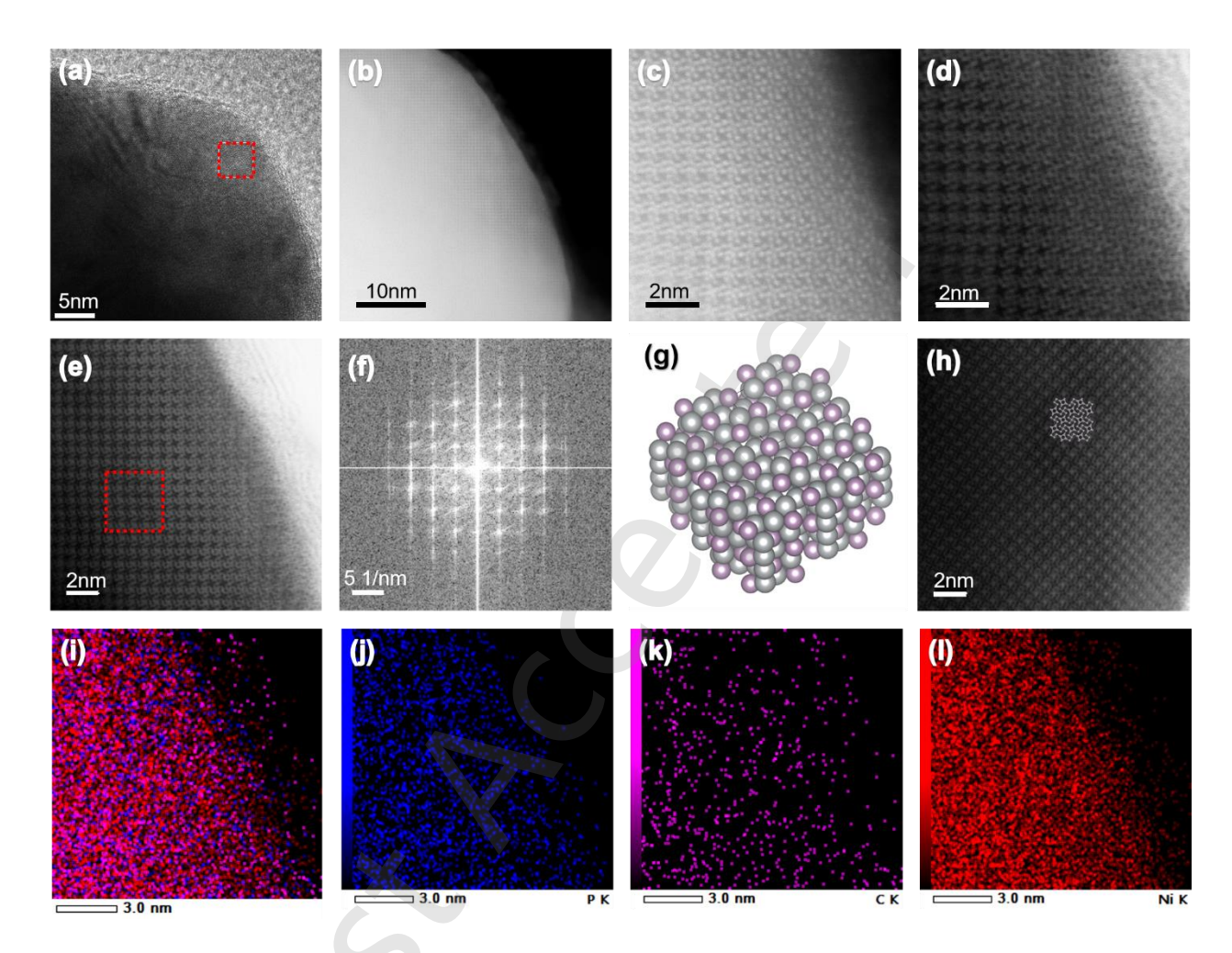


**Fig. 6** Microscopic characterization of NP@C-900 product. (a) TEM image, (b-e) High-angle annular dark-field (HAADF) and annular bright-field (ABF) images of scanning transmission electron microscopy (STEM) of the material. (f) Fourier transform diffraction analysis of the area shown in Fig. 6e. (g) the atomic structure model and (h) corresponding STEM images of Ni12P5. (i-l) Corresponding element mapping results of O, P, C, and Ni.

The local electronic and geometric structure of Ni sites in NP@C was probed using X-ray absorption spectroscopy, combining XANES and EXAFS techniques for comprehensive analysis. Fig. 7a shows the XANES spectra corresponding to the Ni edge of NP@C as a reference. The

absorption edge of NP@C shifts towards higher energy (blue shift) relative to Ni foil, indicating that

Ni is in a higher oxidation state in the carrier. If the spectral line of NP@C is smoother and the

EXAFS oscillation is weak, combined with the previous analysis, nickel is highly dispersed in the

amorphous carbon. In Fig. 7b, the intensity of the front peak of NP@C is significantly higher than

that of Ni foil. There is a lack of a large number of neighboring Ni atoms around Ni, and Ni on its

surface is coordinated with light atoms. Combined with the EDS results, Ni is coordinated with P

atoms. The main peak appears at 2.1-2.3 Å in the figure. Analyzed in combination with the crystal

structure, this time it is Å Ni-P bond, and the bond length of the Ni-P bond is approximately 2.1-2.3

Å, corresponding to the phosphide phase dominated by covalent bonds, with coordination numbers

of 4-6. The bond length of the Ni-Ni bond is approximately 2.5-2.7 Å, which is 8-12.

In Fig. 7(c, d), the densities of state of both samples are not near the Fermi level (0 eV), indicating the existence of density of state at the Fermi level. There is no obvious band gap. The material is metallic or semi-metallic. The material mainly has conductivity loss due to free electron migration. There is a sharp density of state peak formed by the 3d orbitals of Ni near the Fermi level. Meanwhile, the carbon matrix contributes wide peaks within the range of -10 eV to -5 eV, indicating that it has both conductance loss, magnetic loss and dielectric loss of the NP@C nanomaterials. The synergistic effect of this multi-loss mechanism enables it to have a relatively low reflectivity over a wide frequency band. Especially at a specific thickness, efficient wave absorption can be achieved through impedance matching. The absolute value of the state density of the NP@C samples near the Fermi level is as high as -200 to 200, showing typical metallic properties, with a high concentration of free carriers and dominant conductive losses. The DOS of NP@C is asymmetric near the Fermi level, the density of states fluctuates greatly in the high energy region, the spin polarization characteristics are more prominent, and the spin transitions related to magnetic domains may increase the mid and high frequency magnetic loss; The magnetic domain effect of the sample is relatively weak, and the loss is mainly based on the conductivity mechanism. Its reflectance curve

may weaken and the reflectance decreases at high frequencies, but at low frequencies, the reflectance is relatively high because EM waves have difficulty penetrating the material surface. In addition, due to the lack of magnetic element contribution, the magnetic loss of the sample is negligible, resulting in the absorption performance being mainly dependent on conductive loss, and band adaptability and absorption efficiency being weaker than NP@C.

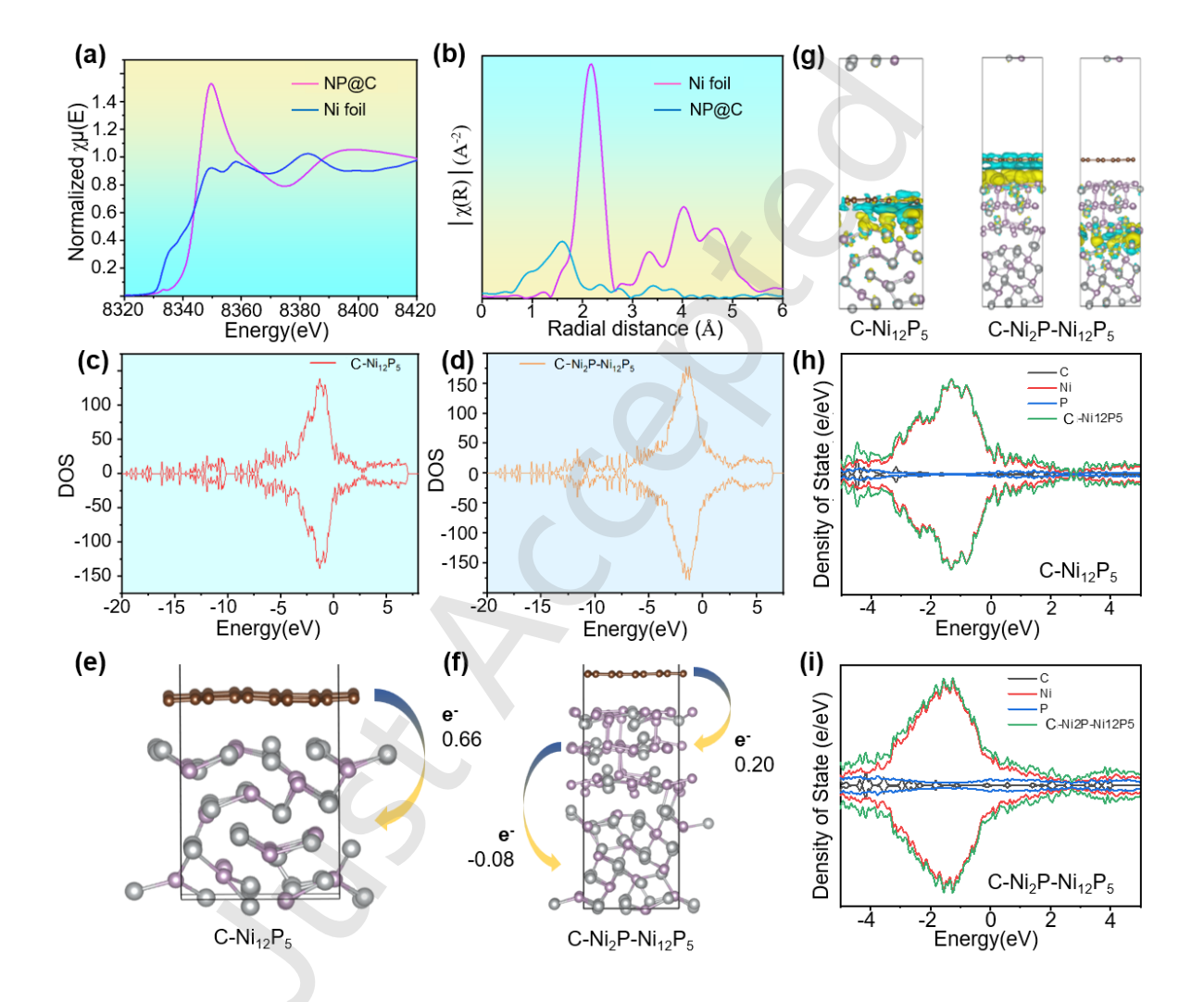


**Fig. 7** The difference in charge density of NP@C material is investigated by DFT calculations. (a) X-ray absorption near edge structure (XANES) and extended X-ray absorption fine structure (EXAFS) spectra. The density of states (DOS) of (c, h) C-Ni<sub>12</sub>P<sub>5</sub> and (d, i) C-Ni<sub>2</sub>P-Ni<sub>12</sub>P<sub>5</sub> calculated through density functional theory (DFT). Atomic structures of (e) C-Ni<sub>12</sub>P<sub>5</sub> and (f) C-Ni<sub>2</sub>P-Ni<sub>12</sub>P<sub>5</sub>. (g) Differential charge density map of C-Ni<sub>12</sub>P<sub>5</sub> and C-Ni<sub>2</sub>P-Ni<sub>12</sub>P<sub>5</sub>.

The difference in charge transfer reflects the influence of electronic behavior between the

Journal of Advanced Ceramics

https://mc03.manuscriptcentral.com/jacer

interfaces of different materials on the dissipation of EM wave energy [40]. The lower charge transfer value (0.66 e) of C-Ni<sub>12</sub>P<sub>5</sub> indicates that electrons are enriched in a specific area at the interface, which may enhance the conductivity of the material and reduce resistance loss (Fig. 7e). This charge distribution will promote the conduction of EM waves within the material, reduce reflection, and thereby enhance the absorption efficiency of EM waves. However, if the charge is overly localized, it may cause local concentration of the electric field, resulting in an increase in dielectric loss. The lower charge transfer value (0.20 e) of C-Ni<sub>2</sub>P-Ni<sub>12</sub>P<sub>5</sub> in Fig. 7f indicates that electron transfer at the interface is relatively efficient, with a small interfacial potential barrier, suggesting that EM dissipation may be facilitated through a dielectric polarization mechanism. In this case, the reflection and transmission of EM waves at the interface tend to be balanced, and the energy loss may mainly be dielectric relaxation or dipole polarization, which is suitable for wideband EM wave absorption applications. The negative charge transfer of C-Ni<sub>2</sub>P-Ni<sub>12</sub>P<sub>5</sub> implies the loss of electrons from the interface region, which may lead to the formation of charge defects or local electric field distortion at the interface. This characteristic can promote the multi-path dissipation of EM wave energy by enhancing the interfacial polarization effect or introducing defect states, and can be absorbed through defect-induced electronic transitions or interfacial resonance. Negative charge transfer can also suppress the overall conductivity of the material, increase eddy current loss, and promote its absorption of EM waves in the high-frequency band.

In Fig. 7g, the different color areas reflect the differences in charge density. The distribution of the yellow and blue regions in the C-Ni<sub>12</sub>P<sub>5</sub> system indicates the existence of an uneven distribution of charges, which is conducive to the formation of electric dipoles. Under the influence of EM waves, these electric dipoles will attempt to align with the direction of the electric field, constantly flipping and adjusting their directions, thereby generating polarization losses, converting EM energy into thermal energy and enhancing the absorption of EM waves. The C-Ni<sub>2</sub>P-Ni<sub>12</sub>P<sub>5</sub> system has a multilayer structure, and the charge density distribution between different layers is different, which

will cause multiple reflections and refractions of EM waves between the layers. During each reflection and refraction process, polarization loss and conductance loss occur due to charge polarization and charge transfer at the interface. At the interfaces of different layers, charges are redistributed to form electric dipoles and generate electron migration to form current, thereby absorbing EM wave energy.

The electronic states of Ni and P in C-Ni<sub>12</sub>P<sub>5</sub> exhibit relatively high-density values near the Fermi level, indicating that the material has significant electronic activity in this energy region (Fig. 7h). The hybridization of the p orbitals of Ni and the p/d orbitals of p may form extensive band overlaps, enhancing the electrical conductivity of the material. High electrical conductivity usually corresponds to lower resistance loss, which is conducive to the conduction of EM waves within the material and energy dissipation. However, the state density near the Fermi level is overly concentrated, which may lead to electronic localization, limit the exertion of polarization ability, and thereby weaken the contribution of dielectric loss. The C-Ni<sub>2</sub>P-Ni<sub>12</sub>P<sub>5</sub> heterostructure, whose density of states distribution shows that the electronic states of N and P extend over a wider energy range, especially with multiple hybrid peaks near the Fermi level (Fig. 7i). This characteristic indicates that band reconstruction at heterogeneous interfaces may introduce interface polarization centers or defect-induced local states. These additional electronic states can significantly enhance dielectric loss through dipole polarization or defect-related electronic transitions. Meanwhile, due to the transfer of negative charges, the loss of electrons at the interface will form charge defects or local electric field distortions, further promoting the interface polarization effect [53]. The band matching characteristics of heterogeneous structures may optimize the impedance matching of materials.

To investigate the far-field EM wave absorption performances in practical applications, different NP@C absorbers were simulated in the form of coatings by the CST Studio Suite. From a 3D RCS diagram (Fig. 8(a-c)), the radar scattering signal of the NP@C-1000 sample was weaker than that of other NP@C absorbers, implying the appropriate EM absorption for NP@C-1000. In addition, RCS

curves (Fig. 8d) indicate the scattered aera in different incident angular. As expected, the minimum RCS value of NP@C-1000 reaches -21.94 dBm<sup>2</sup>. In short, the stable RCS curve of NP@C-1000 under various incident angles and the simulation results that align with the experimental absorption characteristics indicate that NP@C-1000 holds significant potential for practical applications in microwave absorption.

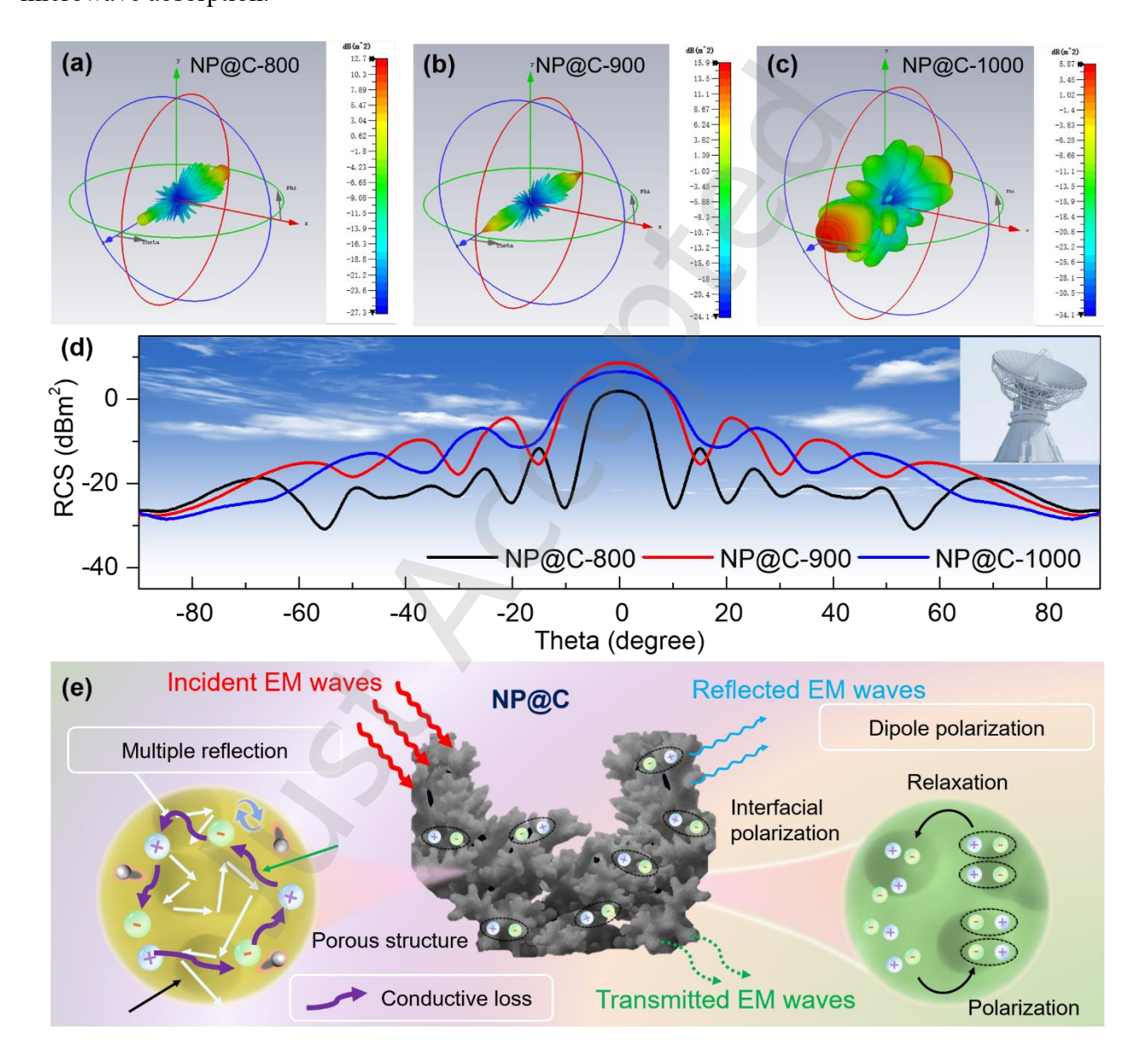


**Fig. 8** 3D radar scattering wave signals of (a) NP@C-800, (b) NP@C-900 and (c) NP@C-900. (d) RCS simulation curves of different NP@C nanocomposites at scanning angle from −90° to 90°. (e) Schematic illustrations of microwave absorption performances in coralloid NP@C products.

In Fig. 8e, the EM wave absorption mechanism of the coral-inspired NP@C absorber is primarily

Journal of Advanced Ceramics https://mc03.manuscriptcentral.com/jacer attributed to its multi-component heterostructure and hierarchical architecture, which work synergistically to enhance EM energy dissipation through conductive, dielectric, and magnetic loss mechanisms. The composite material consists of Ni nanoparticles exhibiting a Ni<sub>12</sub>P<sub>5</sub> core/Ni<sub>2</sub>P shell heterostructure, uniformly dispersed within an amorphous carbon matrix. The distinct crystallographic orientation and interfacial coupling within this system contribute to enhanced EM loss across multiple scales. Theoretical calculations indicate that the charge transfer (0.66 e) occurring at the C-Ni<sub>12</sub>P<sub>5</sub> interface significantly improves conductive loss by facilitating electron migration through the interconnected carbon framework. Concurrently, the C-Ni<sub>2</sub>P-Ni<sub>12</sub>P<sub>5</sub> heterostructure promotes interfacial polarization and the formation of defect states due to negative charge redistribution (-0.20 e), thereby enhancing dipole polarization and relaxation losses associated with structural defects. Electron structure analysis further reveals that the coexistence of sharp Ni 3d orbital peaks near the Fermi level and broad electronic states from the carbon matrix enables dual-loss mechanisms: Ni-derived electronic states contribute to spin-related magnetic loss processes, such as natural resonance and exchange resonance, while the conductive carbon network supports Ohmic loss via Joule heating. In total, the thermally processed NP@C composite exhibits a biomimetic coral-like architecture that establishes an interconnected conductive network for EM waves. This network facilitates the transformation of EM energy into electrical currents while simultaneously creating extended pathways for electron transport, thereby enhancing conductive dissipation [54]. Furthermore, the porous design of the material amplifies the multi-reflections and scattering phenomena of incident EM waves [55]. By harmonizing microwave attenuation mechanisms across multiple scales, the absorber achieves synergistic improvements in energy dissipation, impedance matching, and EM field concentration, resulting in broad bandwidth absorption performance. Overall, the NP@C absorber integrates multi-scale EM loss mechanisms, delivering superior wideband absorption with strong attenuation capabilities.

## 4 Conclusions

In summary, magnetic MOF-derived carbon materials were prepared by using self-template and restricted conversion strategies. Through precise component and structural design, a perfect magnetoelectric balance has been achieved, demonstrating excellent absorbing capacity. The findings indicate that the pyrolysis temperature has a profound impact on the crystallinity and morphology of the material. The Ni<sub>12</sub>P<sub>5</sub>/Ni<sub>2</sub>P heterostructure and spherical carbon matrix formed at 1000 °C provide abundant heterointerfaces and conductive networks for effective EM wave interaction. The moderate carbon defect level of NP@C-1000 achieves an optimal balance between conductance loss and interfacial polarization, while the synergistic effect of Ni nanoparticles embedded in the carbon matrix enhances natural resonance and eddy current loss. NP@C-1000 exhibits full-band effective absorption (RL < -10 dB) across the 4.1 GHz (13.9-18.0 GHz) range with a minimum RL of -54.1 dB at 16.1 GHz (1.37 mm), significantly surpassing other samples due to its optimized impedance matching and the synergistic action of multiple loss mechanisms. The charge transfer (0.66 e) at the Ni<sub>12</sub>P<sub>5</sub>/carbon interface enhances electrical conductivity, whereas the relatively low charge transfer (0.20 e) within the C-Ni<sub>2</sub>P/Ni<sub>12</sub>P<sub>5</sub> heterostructure promotes dielectric polarization, further elucidating its broadband absorption mechanism. In summary, the NP@C-1000 sample demonstrates remarkable potential for wideband EM wave absorption through structural design and compositional control, offering new insights into the development of high-performance absorbing materials.

#### Availability of data and materials

The data that support the findings of this study are available from the corresponding author upon reasonable request.

#### **Competing interests**

#### **Author contributions**

Y. Liu designed the experiments and wrote the manuscript. M. Li and R. Li conducted material synthesis and performed SEM, XRD, VSM, Raman characterizations and electromagnetic analysis.

Y. Qing and B. Fan polished the English grammar and provided the Resources and Project administration. L. Wang conducted theoretical calculation.

## Acknowledgements

This work was financially supported by the National Natural Science Foundation of China (52572086), Scientific and Technological Innovation Talents in Colleges and Universities in Henan Province (22HASTIT001), and Henan Province Natural Science Foundation Outstanding Youth Fund Project (242300421009).

#### References

- [1] Tao JQ, Yan Y, Zhou JT, et al. Anionic high-entropy doping engineering for electromagnetic wave absorption. Nat Commun 2025, 16: 3163.
- [2] Zhao QQ, Zhang TY, Ma CQ, et al. In-situ growth of metal organic framework on hollow graphene foam for high-efficiency microwave absorption. J Mater Sci Technol 2025, 235: 251-260.
- [3] Yu GY, Shao GF, Xu RP, et al. Metal-organic framework-manipulated dielectric genes inside silicon carbonitride toward tunable electromagnetic wave absorption. 2023, **19**: 2304694.
- [4] Xiao JX, Zhan BB, He MK, *et al.* Mechanically robust and thermal insulating nanofiber elastomer for hydrophobic, corrosion-resistant, and flexible multifunctional electromagnetic wave absorbers. *Adv Funct Mater* 2025, **14**: 2419266.

- [5] Hui SC, Chen Q, Tao K, *et al.* Highly mixed index facet engineering induces defect formation and converts the wave-transmissive mott insulator NiO into electromagnetic wave absorbent. *Adv Mater* 2025, **37**: 2415844.
- [6] Xing L, Cheng H, Li Y, *et al.* Simultaneous manipulation of constituent and structure toward MOFs-derived hollow Co<sub>3</sub>O<sub>4</sub>/Co/NC@MXene microspheres via pyrolysis strategy for high-performance microwave absorption. *Chem Eng J* 2024, **487**: 150729.
- [7] Feng WX, Liu YY, Bi YX, et al. Recent advancement of magnetic MOF composites in microwave absorption. Synth Met 2023, **294**: 117307.
- [8] Zhang X, Tian XL, Wu N, *et al.* Metal-organic frameworks with tunable conductivity for microwave absorption. *Sci Adv* 2024, **10**: 6498.
- [9] Zhang F, Li N, Shi JF, *et al.* Recent progress on carbon-based microwave absorption materials for multifunctional applications: A review. *Compos part B-ENG* 2024, **283**: 111646.
- [10] Zhao T, Zheng T, Lan D, *et al.* Self-assembly tungsten selenide hybrid ternary MOF derived magnetic alloys via multi-polarization to boost microwave absorption. *Nano Res* 2024, **17**: 1625-1635.
- [11] Qu N, Xu G, Liu Y, et al. Multi-scale design of metal-organic framework metamaterials for broad-band microwave absorption. Adv Funct Mater 2024, 1: 2402923.
- [12] Ren SN, Yu HJ, Wang L, *et al.* State of the art and prospects in metal-organic framework-derived microwave absorption materials. *Nano Micro Lett* 2022, **14**: 14:68.
- [13] Wang MQ, Cao MS. Perspectives on metal-organic framework-derived microwave absorption materials. *J Mater Sci Technol* 2025, **214**: 37-52.
- [14] Geng TB, Yu GY, Shao GF, *et al.* Enhanced electromagnetic wave absorption properties of ZIF-67 modified polymer-derived SiCN ceramics by in situ construction of multiple heterointerfaces. 2023, **42**: 1635-1644.

- [15] Zheng JJ, Lan D, Zhang SJ, *et al.* Zeolite imidazolate framework derived efficient absorbers: From morphology modulation to component regulation. *J Alloys Compd* 2025, **1010**: 177092.
- [16] Qu N, Sun HX, Sun YY, et al. 2D/2D coupled MOF/Fe composite metamaterials enable robust ultra–broadband microwave absorption. *Nat Commun* 2024, **15**: 5642.
- [17] Wei KX, Shi Y, Tan X, et al. Recent development of metal-organic frameworks and their composites in electromagnetic wave absorption and shielding applications. Adv Colloid Interface Sci 2024, 332: 103271.
- [18] Li LT, Liu JR, Pan F, *et al.* Structural engineering of rare earth metal-organic frameworks derivatives with high anisotropy for high-efficiency electromagnetic wave absorption. *Chem Eng J* 2024, **481**: 148383.
- [19] Hu JH, Liu MZ, Zhai YQ, *et al.* Metal organic frameworks-derived (MOFs) square Fe@C crystals dotted C composite nanofibers for enhanced electromagnetic wave absorption performance. *Nanoscale* 2025, **17**: 16432-16446.
- [20] Gao ZG, Iqbal A, Hassan T, *et al.* Tailoring built in electric field in a self assembled zeolitic imidazolate framework/MXene nanocomposites for microwave absorption. *Adv Mater* 2024, **36**: 19.
- [21] Huang MQ, Wang L, Pei K, *et al.* Heterogeneous interface engineering of Bi-metal MOFs-derived ZnFe<sub>2</sub>O<sub>4</sub>-ZnO-Fe@C microspheres via confined growth strategy toward superior electromagnetic wave absorption. *Adv Funct Mater* 2023, **34**: 3.
- [22] Wang P, Gai LX, Hu B, *et al.* Topological MOFs deformation for the direct preparation of electromagnetic functionalized Ni/C aerogels with good hydrophobicity and thermal insulation. *Carbon* 2023, **212**: 118132.
- [23] Mao LJ, Qian JJ. Interfacial Engineering of Heterogeneous Reactions for MOF on MOF Heterostructures. *Small* 2023, **20**: 20.
- [24] Chen JL, Wang L, Shen B, *et al.* Biomass-based Co/C@Carbon composites derived from MOF-modified cotton fibers for enhanced electromagnetic attenuation. *Carbon* 2023, **210**: 118035.

- [25] Liu G, Zhu PB, Teng J, et al. Optimizing MOF derived electromagnetic wave absorbers through gradient pore regulation for pareto improvement. Adv Funct Mater 2025, **35**: 2413048.
- [26] Gao Z.G, Iqbal A, Hassan T, *et al.* Texture regulation of metal-organic frameworks, Microwave absorption mechanism-oriented structural optimization and design perspectives. *Adv Sci* 2022, **9**: 2204151.
- [27] Huang MQ, Wang L, Pei K, et al. Multidimension-controllable synthesis of MOF-derived Co@N-doped carbon composite with magnetic-dielectric synergy toward strong microwave absorption. Small 2020, 16: 2000158.
- [28] Deng B, Xiang Z, Xiong J, et al. Sand-wich-Like Fe&TiO<sub>2</sub>@C nanocomposites derived from MXene/Fe-MOFs hybrids for electromagnetic absorption. Nano-Micro Lett 2020, 12: 55.
- [29] Zhao B, Du Y, Yan Z, et al. Structural defects in phase-regulated high-entropy oxides toward superior microwave absorption properties. Adv Funct Mater 2023, 33: 2209924.
- [30] Li Y, Qing YC, Yao H, et al. A novel plasma-sprayed Ti<sub>4</sub>O<sub>7</sub>/carbon nanotubes/Al<sub>2</sub>O<sub>3</sub> coating with bifunctional microwave application. J Colloid Interface Sci 2023, **645**: 165-175
- [31] Hao B, Zhang Y, Si HX, *et al.* Multiscale design of dielectric composites for enhanced microwave absorption performance at elevated temperatures. *Adv Funct Mater* 2025, **35**: 2423897.
- [32] Zhang Y, Si HX, Dai ZY, et al. Subwavelength-scale graphene aerogel powders for efficient microwave absorption composites with improved mechanical strength. Chem Eng J 2025, 505: 159118.
- [33] Zhang D, Zhou XM, Liu JA, *et al.* Selective synthesis of Ni<sub>12</sub>P<sub>5</sub> and Ni<sub>2</sub>P nanoparticles: Electronic structures, magnetic and optical properties. *Mater Sci Eng B* 2021, **273**: 115389.
- [34] Aziam H, Indris S, Knapp M, *et al.* Synthesis, Characterization, Electrochemistry, and In Situ X- ray Diffraction Investigation of Ni<sub>3</sub>(PO<sub>4</sub>)<sub>2</sub> as a Negative Electrode Material for Lithium-Ion Batteries. *ChemElectroChem* 2020, 7: 3866-3873.

- [35] Pan F, Ning M, Li Z, et al. Sequential architecture induced strange dielectric-magnetic behaviors in ferromagnetic microwave absorber. Adv Funct Mater 2023, 33: 2300374.
- [36] Cao MS, Shu J, Wen B, *et al.* Genetic dielectric genes inside 2D carbon-based materials with tunable electromagnetic function at elevated temperature. *Small Struct* 2021, **2**: 2100104.
- [37] Wang ZY, Li ZC, Li B, *et al.* Functional carbon springs enabled dynamic tunable microwave absorption and thermal insulation. *Adv Mater* 2024, **36**: 2412605.
- [38] Zhao ZH, Qing YC, Kong L, et al. Advancements in microwave absorption motivated by interdisciplinary research. Adv Mater 2024, 36: 2304182.
- [39] Li N, Zong Z, Zhang F, et al. Barium ferrite with high anisotropy for ultra-broadband microwave absorption. Adv Funct Mater 2025, 35: 2414694.
- [40] Chen F, Chen FQ, Ding JQ, et al. CoNi alloy nanoparticles embedded in metal-Organic framework-derived carbon for the highly efficient separation of xenon and krypton via a charge-transfer effect. *Angew Chem Int Ed* 2021, **60**: 2431–2438.
- [41] Lin HR, Green M, Xu LJ, et al. Microwave Absorption of Organic Metal Halide Nanotubes. Adv Mater 2020, 7: 1901270.
- [42] Chen P, He SB, Zou ZK, et al. Intelligent hydrogels enabled large-scale variability in continuously tunable microwave absorption. Adv Funct Mater 2025, 1: 2506308.
- [43] Yuan K, Han D, Liang J, et al. Microwave induced in-situ formation of SiC nanowires on SiCNO ceramic aerogels with excellent electromagnetic wave absorption performance. *J Adv Ceram* 2021, **10**: 1140-1151.
- [44] Xu HL, Zhan HY, Xu ZJ, *et al.* Sandwich-like CNTs/carbon@Si<sub>3</sub>N<sub>4</sub> porous foam for temperature-insensitive electromagnetic wave absorption. *Adv Funct Mater* 2025, **1**: 2421242.
- [45] He MK, Zhong X, Lu XH, *et al.* Excellent low-frequency microwave absorption and high thermal conductivity in polydimethylsiloxane composites endowed by hydrangea-like CoNi@BN heterostructure fillers. *Adv Mater* 2024, **36**: 2410186.

- [46] Xiao JX, Zhan BB, He MK, *et al.* Interfacial polarization loss improvement induced by the hollow engineering of necklace-like PAN/Carbon nanofibers for boosted microwave absorption. *Adv Funct Mater* 2025, **35**: 2316722.
- [47] Zhang Y, Si HX, Dai ZY, et al. Subwavelength-scale graphene aerogel powders for efficient microwave absorption composites with improved mechanical strength. Chem Eng J 2025, 505: 159118.
- [48] Niu H, Jiang X, Xia Y, *et al.* Construction of hydrangea-like core–shell SiO<sub>2</sub>@Ti<sub>3</sub>C<sub>2</sub>T<sub>x</sub>@CoNi microspheres for tunable electromagnetic wave absorbers. *J Adv Ceram* 2023, **12**: 711-723.
- [49] Cao MS, Terrones M, Carbon-based electromagnetic functional materials: a virtual special issue. *Carbon* 2024, **218**: 118706.
- [50] Zhao B, Yan Z, Du Y, et al. High-Entropy enhanced microwave attenuation in titanate perovskites. Adv Mater 2023, 35: 2210243.
- [51] Li Y, Qing YC, Zhang Y, et al. Simultaneously tuning structural defects and crystal phase in accordion-like  $Ti_xO_{2x-1}$  derived from  $Ti_3C_2T_x$  MXene for enhanced electromagnetic attenuation. J Adv Ceram 2023, 12: 1946-1960.
- [52] Zeng X, Jiang X, Ning Y, et al. Construction of dual heterogeneous interface between zigzag-like Mo–MXene nanofibers and small CoNi@NC nanoparticles for electromagnetic wave absorption.

  J Adv Ceram 2023, 12: 1562-1576.
- [53] Liu H, Li XQ, Zhao XY, et al. Large annular dipoles bounded between single-atom Co and Co cluster for clarifying electromagnetic wave absorbing mechanism. Adv Funct Mater 2023, 33: 2304442.
- [54] Huang XG, Guan JP, Feng YJ, *et al.* Mn and O defect modulation in birnessite creates multiplicate polyhedra to improve dielectric and magnetic losses. *Cell Rep Phys Sci* 2025, **6**: 102350. [55] Huang XG, Yu GY, Quan B, *et al.* Harnessing Pseudo-Jahn–Teller disordering of monoclinic birnessite for excited interfacial polarization and local magnetic fomains. 2023, **7**: 2300045.

# **Graphical abstract**

